

# Visible spectrum of highly charged ions: The forbidden optical lines of Kr, Xe, and Ba ions in the Ar I to Kr I isoelectronic sequence

J.R. Crespo López-Urrutia, P. Beiersdorfer, K. Widmann, and V. Decaux

**Abstract:** We present experimental data on visible transitions in highly charged ions observed in the Lawrence Livermore National Laboratory (LLNL) electron beam ion traps, including results from lines within the ground-state configuration and the first excited configuration. Measurements of lines produced by Kr ( $q = 11+$  to  $22+$ ), Xe ( $q = 18+$  to  $35+$ ), and Ba ( $q = 28+$  to  $36+$ ) ions, corresponding mainly to  $3s^\ell 3p^m 3d^n$  configurations, were carried out. The ionization stages were determined experimentally by sweeping the electron beam energy over the ionization threshold of each species. We propose possible identifications for the lines with the help of simple atomic structure calculations. However, most observed lines remained unidentified, demonstrating that the understanding of visible spectra from highly charged ions, even if obtained under nearly “ideal” experimental conditions, is still in its infancy. These spectral data may be useful for the diagnostics of magnetically confined plasmas and may set the stage for future measurements of radiative lifetimes. In our experiments, we used the emission from visible lines to image the intersection of the electron beam with a beam of neutral atoms injected into the trap at a right angle as well as the ion cloud in the trap. Under some conditions, the diameter of the ion cloud may be an order of magnitude larger than that of the electron beam.

PACS Nos.: 32.30Jc, 39.30+w, 52.59Rz

**Résumé :** Nous présentons des résultats expérimentaux sur des transitions dans le visible d'ions hautement chargés, telles qu'observées dans des pièges ioniques à faisceau électronique, incluant des résultats de lignes présentes dans les configurations du fondamental et du premier niveau excité. Nous avons mesuré des lignes produites par du Kr ( $q = 11+$  à  $22+$ ), du Xe ( $q = 18+$  à  $35+$ ) et du Ba ( $q = 28+$  à  $36+$ ), correspondant surtout aux configurations  $3s^\ell 3p^m 3d^n$ . Le niveau d'ionisation est déterminé expérimentalement par un balayage en énergie du faisceau électronique au dessus du seuil d'ionisation de chaque type d'ion. Sur la base de calculs simples de structure atomique, nous proposons une identification possible des lignes. Cependant, la majorité des lignes demeure sans identification, démontrant que nous en sommes encore aux balbutiements dans l'identification des lignes dans le visible

Received 16 May 2002. Accepted 16 August 2002. Published on the NRC Research Press Web site at <http://cjp.nrc.ca/> on 9 January 2003.

J.R. Crespo López-Urrutia, P. Beiersdorfer,<sup>1</sup> K. Widmann, and V. Decaux.<sup>2</sup> Lawrence Livermore National Laboratory, University of California, P.O.B. 808, Livermore, CA 94551, U.S.A.

<sup>1</sup>Corresponding author (e-mail: [beiersdorfer@llnl.gov](mailto:beiersdorfer@llnl.gov)).

<sup>2</sup>Present address: PRIMEX, San Leandro, CA 94577, U.S.A.

provenant d'ions hautement chargés, même dans des conditions expérimentales *idéales*. Ces données spectrales peuvent être utiles dans le diagnostic de plasmas confinés et mettent la table pour de futures mesures de temps de vie radiatifs. Dans notre montage, nous utilisons les émissions dans le visible pour imager l'intersection entre le faisceau électronique et le faisceau d'ions neutres injectés à angle droit aussi bien que le nuage ionique dans le piège. Dans ces conditions, le diamètre du nuage ionique peut être un ordre de grandeur plus grand que le faisceau électronique.

[Traduit par la Rédaction]

## 1. Introduction

Visible light emitted by highly charged ions has important applications in the diagnostics of laboratory and astrophysical plasmas. Many resonance lines of highly charged ions are in the X-ray region, but some forbidden transitions from the same ions appear within the visible range. Compared to conventional X-ray techniques, standard optical methods offer higher spectral and spatial resolution, larger collection solid angles, and higher detection efficiency. For astrophysics, it is also important that, because of the low absorption by the interstellar medium in the visible range, the distances to stellar objects observable in the visible spectrum in many cases surpass the limits of soft X-ray and VUV methods. Earth-based telescopes can be used to detect this visible radiation from highly charged ions without the need of space-based instruments in the X-ray and XUV–VUV regions. Forbidden optical transitions from highly charged ions have been detected in the Sun before X-rays measurements were performed; the so-called “coronal” visible lines thus gave the first evidence for such highly charged ions in the Sun. A well-known example is the Fe XIV forbidden line at 5303 Å; the first observation of this strong line in the solar corona dates back to 1869 [1]. More forbidden lines of ions with  $2s^\ell 2p^m$ ,  $2s^2 2p^4$ ,  $2s^2 2p^3 3d$  or similar configurations have been observed in astrophysical sources (see, e.g., the early compilation by Swings [2] or the survey by Wagner and House [3]), in magnetically confined plasmas [4–6], and in ions extracted from electron cyclotron resonance (ECR) sources [7]. The identification of some predicted lines in the V-like and Ti-like ions  $\text{Ba}^{33+,34+}$  and  $\text{Xe}^{32+,33+}$  in an electron beam ion trap at the National Institute of Science and Technology (NIST) by Morgan et al. [8] showed for the first time the possibilities of such an instrument for the study of optical transitions in ions of very high charge states. Electron beam ion traps have since been very helpful in finding the footprints of highly charged ions in the visible range along various isoelectronic sequences [9–13].

A very common characteristic of forbidden optical lines in highly charged ions is that they are produced by intra-configuration transitions, mostly due to the presence of a metastable level within the ground-state configuration. There are many possible electronic configurations with metastable levels. Particularly important are those with open  $p$  or  $d$  subshells, or also a  $p$ -subshell or  $d$ -subshell with one electron hole and one electron promoted to the next higher subshell or shell. In the latter cases, combinations of the orbital momenta of the electron and the hole exist that results in a large total angular momentum  $J > 1$  of the ion. The decay to the ground state through an electric dipole transition is forbidden, if  $\Delta J > 1$ , or, as it is the case within the ground-state configuration when no parity change is possible. Magnetic dipole (M1) and higher order transitions can nonetheless take place. In the absence of faster competing transitions in the VUV or X-ray region and of collisional depopulation, the excited sublevel relaxes by emitting a low-energy photon. In neutral atoms, all these transitions have very small Einstein coefficients and collisional depopulation of the metastable levels is very likely. As the charge state goes up along an isoelectronic sequence, the energy scaling laws shift the spectral range of the lines to higher energies and the transitions rates become larger following a power law. Lines that are in the infrared or microwave region for neutral atoms appear in the visible or UV spectrum for highly charged ions. In plasmas, where the excitation temperature tends to be of the same order of magnitude as the ionization potential of the ions, excitation rates for high-lying levels are larger than for excited states within the ground-state configuration because of the energy mismatch between the average electron

energy and the transition energy and also because they may require a spin-flip process. The metastable levels within low-lying or ground-state configurations are therefore populated mainly by cascades from higher levels making the associated spontaneous transition rate a poor indicator for the intensity of the resulting spectral lines.

In dense laboratory sources, forbidden transitions are quenched through collisions, given the fact that typical forbidden transition rates of the order of several hundred per second are usually lower by several orders of magnitude than the collision frequencies in dense plasmas. As a result, their observation in the high-density regions of laser produced plasmas, for example, is impossible. Tokamak plasmas, on the other hand, have a much lower density and have allowed the observation of many forbidden lines [4–6]. Many of the lines in the present work may be of diagnostic importance for such devices, especially as the deliberate introduction of high- $Z$  material has been suggested as a means for distributing the heat on plasma facing components [14–16]. Under low-density conditions, forbidden magnetic dipole, electric quadrupole (E2), and magnetic quadrupole (M2) lines can appear as strong as electric dipole allowed (E1) transitions, and any of the lines we report in the present work could all be observed provided the appropriate ions are produced in such low-density plasmas.

The identification of visible lines ideally requires an apparatus able to generate a single charge state at precisely controlled excitation conditions. The conditions for observation of this type of transition are best realized in a low-density light source, such as an electron beam ion trap. Such an apparatus is able to produce selectively ions of any charge state, and the collision frequency is comparatively low (electron density  $n_e \leq 10^{12} \text{ cm}^{-3}$ ), as shown in many spectral studies in the X-ray region [17–19]. Furthermore, the spatial confinement of the ions in the trap is well suited for the spectroscopic technique presented here, which combines wide simultaneous spectral coverage, spatial resolution, and large dynamic range. This technique makes possible to survey series of charge states in a short time, and it has successfully been applied to the extreme case of the ground-state hyperfine transitions of H-like  $\text{Ho}^{66+}$  and  $\text{Re}^{74+}$ , where the hyperfine splitting produces lines in the visible range [20,21].

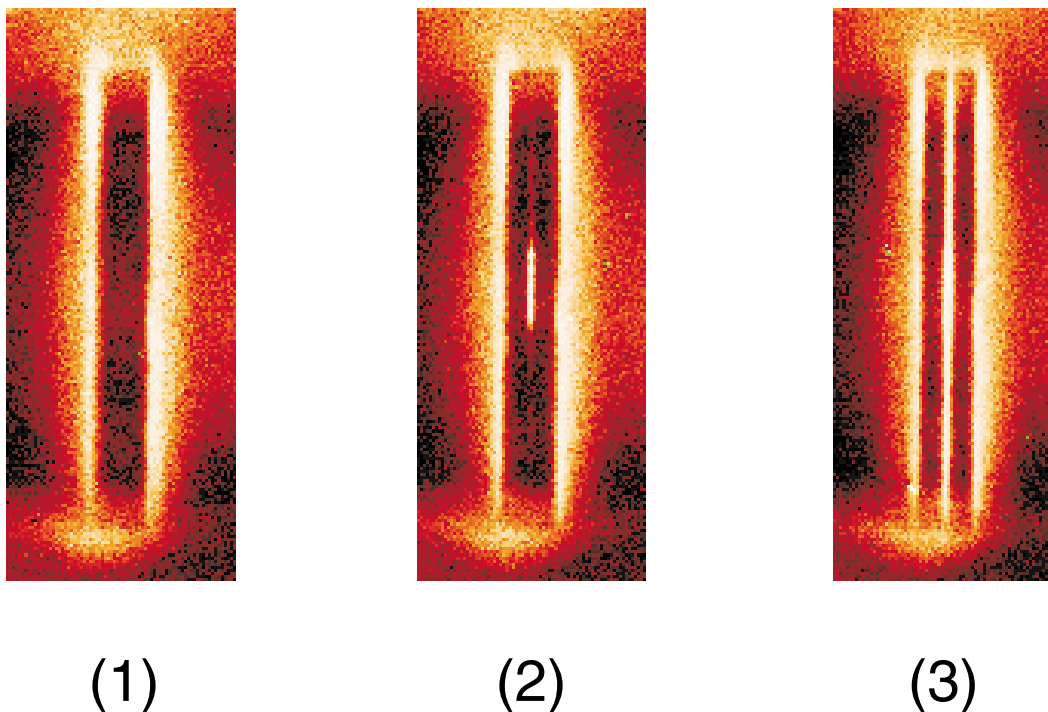
In the following, we apply the sensitivity and speed of this technique mainly to the study of Ba, Xe, and Kr ions with  $3p^m 3d^n$  configuration in the visible wavelength band from about 3800 to 6500 Å, complementing studies in the optical range below 4000 Å and setting the stage for radiative lifetime measurements [22–25].

## 2. Experimental setup

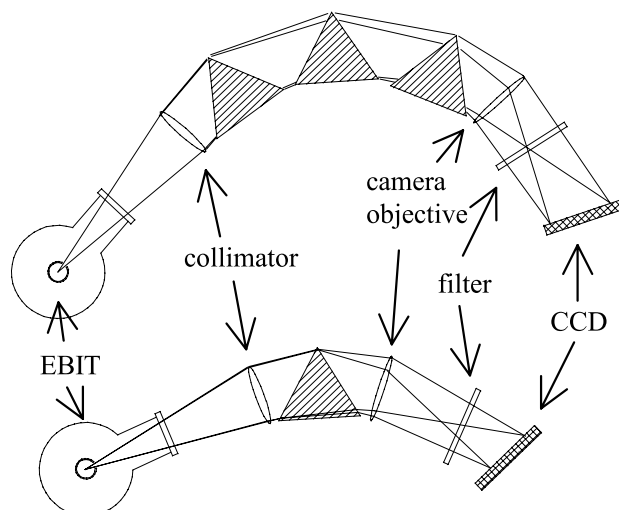
The present measurements were carried out at the Livermore EBIT-II and SuperEBIT electron beam ions traps. These are the second and third electron beam ion traps built following the first electron beam ion trap, dubbed EBIT-I, put into operation in the middle of the 1980s. Ions are produced and stored in an electron beam ion trap by an electron beam of variable energy axially compressed by a high magnetic field produced by a superconductive split-pair magnet with radial access. The ions are confined axially within a potential well produced by three cylindrical electrodes, the so-called drift tubes. The electron beam passes through this electrode assembly, and the ions are trapped inside the so-called middle drift tube, which is slightly negative in relation to the upper and lower drift tubes. Slotted apertures on the side of the middle drift tube allow optical access to the trapped ions. The trap is initially loaded with neutral atoms from an atomic beam on the side of the apparatus or by injecting low-charge state ions generated in a Metal Vapor Vacuum Arc (MeVVA) discharge device, though the latter technique was not used in these experiments. The ion charge state balance is mainly determined by the electron beam energy, but is also influenced by the neutral gas density in the trap through charge-exchange processes and by the evaporative cooling of the trapped ions due to collisions with the neutrals. Periodically the trap contents are dumped by changing the trapping potential to keep a reproducible ion population within the trap and to avoid the slow accumulation of high- $Z$  impurities. Typical cycling times for krypton, xenon, or barium are several seconds.

The first step taken in our experiment was to set up an apparatus for visibly imaging the trap region.

**Fig. 1.** Images of the middle drift tube of SuperEBIT obtained under different operating conditions: (1) electron beam on, no gas injection, trap open; (2) electron beam on, gas injection on, trap open; (3) electron beam on, gas injection on, trap closed. In (2), the region of the trap shows light emission from neutrals and singly ionized atoms excited by the electron beam at its intersection with the gas injector atomic beam. In (3), highly charged ions trapped in the full length of the middle drift tube generate intense light emission from forbidden lines.



A cryogenically cooled charge-coupled device (CCD) camera with an appropriate objective was used [26]. A port with a quartz window on the side of the vacuum chamber allowed direct view of the beam in the trap region through a slotted aperture in the drift tube. Because of the faintness of the radiation of interest, a reduction of background light from external sources was essential. With this apparatus we have studied the trap geometry, the cooling gas injection mechanism, and the spatial distribution of charged states within the trap. Two different light emitting regions appear clearly distinguishable in the images taken: (a) the trap region between the upper and the lower drift tubes, where the highly charged ions are stored, and (b) the overlap of the electron beam with an atomic beam from the cooling gas injector, which crosses the central portion of the trap as illustrated in Fig. 1. The trap potential was turned on and off to confirm these assignments. By changing the drift tube potential, the ions are either trapped or allowed to escape axially. The gas injector flux was also switched on and off to observe its effect. The neutral gas atoms from the gas injector beam emit light when they cross at an angle of  $90^\circ$  the electron beam at the trap center. The electron beam diameter of about  $70 \mu\text{m}$  determines the width of the emitting region; the cold gas injector atomic (or molecular) beam has a diameter of  $\approx 4 \text{ mm}$ , so the overlap is a cylinder of  $4 \text{ mm}$  length by  $70 \mu\text{m}$  diameter. Due to the very fast ionization rate at the beginning of the trapping process, which can take only a few microseconds, the low-momentum transfer to the ions produced in these initial steps, and the comparatively long axial oscillation times in the trap (on the order of tens of microseconds), low-charge state ions do not have enough time to spread from the central region into the ballistically inaccessible regions of the trap. This is borne out by the images. In contrast to this, the trapped ions fill the whole trap length. The trapped ions were stored in a longer cylinder ( $\approx 20 \text{ mm}$ ) with a larger diameter ( $\approx 200 \mu\text{m}$ ). The random process of photon emission from

**Fig. 2.** Different arrangements for the spectrograph used on SuperEBIT and EBIT-II.

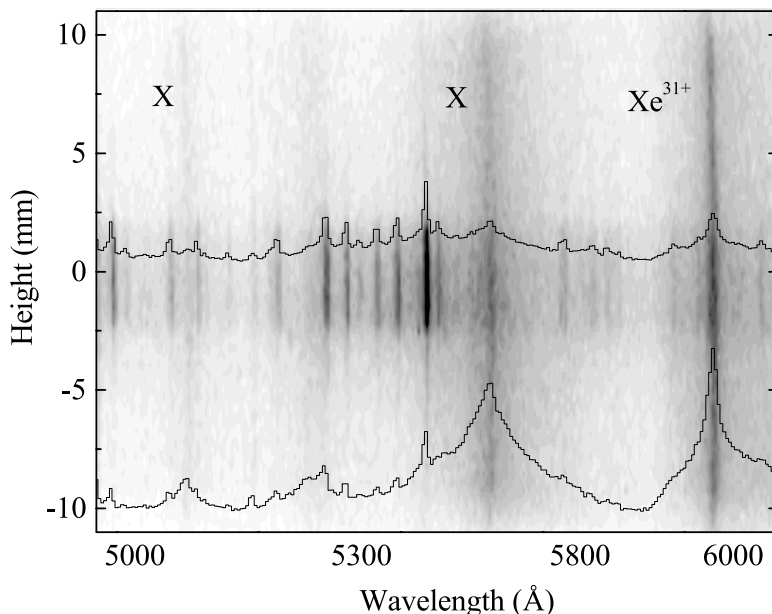
long-lived states provides a convenient means for mapping the spatial distribution of the ions, which extends also outside of the electron beam. Earlier studies by X-ray imaging have used very short-lived transitions excited by the electron beam, thus only reflecting the electron beam size, or more precisely its overlap with the ion cloud, since the ions excited by the beam immediately decay to their ground state, without leaving the excitation region [27,28].

As a second step, a prism spectrograph (manufactured by Steinheil, Munich) was set up as shown schematically in Fig. 2. A stigmatically imaging prism spectrograph was chosen because of its high efficiency, low level of scattered light, and the needs of our geometrical arrangement. This setup differs greatly from the scanning monochromator with photomultiplier tube (PMT) used at the NIST EBIT facility and described in ref. 8 in that (a) it allows simultaneous coverage of the whole visible spectrum, providing much faster data acquisition (typical exposure times ranged from 1 min to 1 h); (b) it also has lower noise: typical PMTs have several tens of counts per second of dark current, versus a few tens of counts per hour for the CCD detector used here, if a single line is recorded on a detector surface of typically 400 pixels (0.5 dark electrons per pixel per hour specification); this amounts to about three orders of magnitude less noise on average; (c) the quantum efficiency of the back-illuminated CCD used on this experiment is as high as 85% in some regions of the visible spectrum and typically around 50% overall and therefore clearly superior to the 10% quantum efficiency usually found with PMTs; and (d) its trap volume is spatially resolved in the vertical and horizontal directions, giving information about the spatial distribution of the ions. The electron beam and the apparatus symmetry axis are aligned vertically. The trap volume is stigmatically imaged by two achromats ( $f_1 = 655$  mm,  $f_2 = 250$  mm, demagnification 2.6 times) onto the focal plane of the spectrograph, where the CCD detector is placed ( $512 \times 512$  or  $1024 \times 1024$  pixels of  $24 \mu\text{m} \times 24 \mu\text{m}$  size length). The narrow trap volume itself replaces the entrance slit of the spectrograph arrangement.

Depending on the number of prisms used in the spectrograph, the region covered can be from several hundred angstroms up to  $3000 \text{ \AA}$  in a single image. The resolution varies accordingly; usually, the dispersion is about  $1.5 \text{ \AA/pixel}$  in the blue region ( $4000 \text{ \AA}$ ),  $5 \text{ \AA/pixel}$  in the green ( $5400 \text{ \AA}$ ), and  $13 \text{ \AA/pixel}$  in the red ( $7000 \text{ \AA}$ ). The best resolution achieved was  $0.6 \text{ \AA/pixel}$ . The spatial resolution depends on the imaging arrangement and can reach  $20 \mu\text{m}$  with an appropriate magnifying lens. The total detection efficiency of the system, taking in consideration a solid angle collection efficiency of  $8 \times 10^{-4}$  (F/9), is around  $2.5 \times 10^{-4}$ .

To minimize background, all possible light sources in the chamber (ion pressure gauges) had to

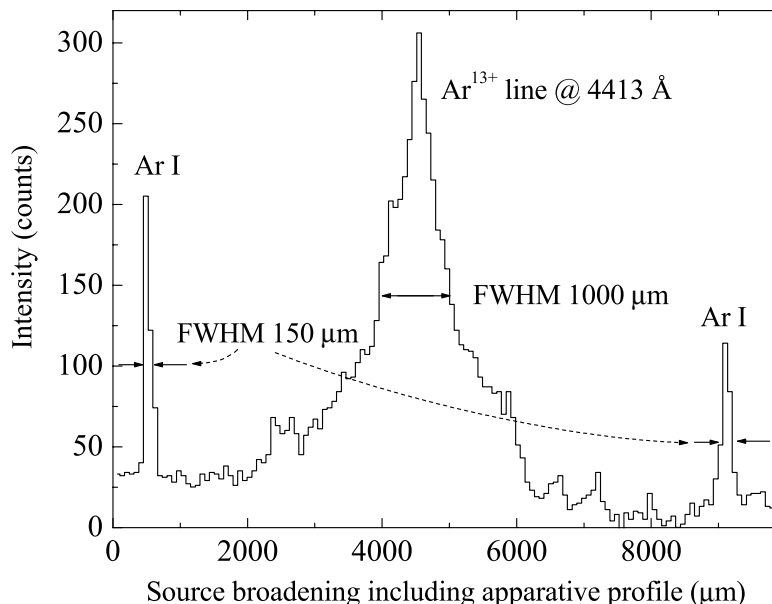
**Fig. 3.** Spectral images obtained on SuperEBIT with Xe at a beam energy of 2210 eV. Lineouts of the central spectrum and the outer spectrum are superimposed. The lines marked with “X” are unidentified transitions from  $\text{Xe}^{q+}$  ions with ( $18 < q < 30$ ). “Height” is the image dimension along the trap axis (vertical). Radiation from allowed optical transitions from neutral as well as singly and doubly charged Xe is emitted mainly at the center region (4 mm) of the trap. Trapped ions in contrast fill the whole trap height (20 mm); the forbidden lines appear accordingly longer.



be turned off. The largest source of background was the thermal radiation from the indirectly heated electron gun cathode. This red and near-IR stray light was reduced by a filter with a 6700 Å cut-off.

The spatial resolution of the spectrograph allowed us to distinguish the two light-emitting regions observed with the previous imaging setup with added spectral resolution: Region A, the trap volume between the upper and the lower drift tubes, where the highly charged ions were stored, and region B, the crossing of the electron beam with the gas injector atomic beam, comprising the central portion of the trap (see Fig. 3 and compare with Fig. 1). Only a few lines appeared in the region B; they were long and correspond mostly to M1 transitions within the ground state of high- $Z$  ions with  $3d^n$  configurations and mid- $Z$  ions with  $2p^m$  configurations (e.g., from  $\text{Ar}^{9+}$ ,  $\text{Ar}^{13+}$ , and  $\text{Ar}^{14+}$ ). The central region A of the trap (4 mm) displayed many lines from neutrals and singly ionized atoms from the cooling gas, with a short and narrow spatial profile. Here, electron collisional excitation and fast radiative decay of the neutral atoms take place and the electron beam diameter of 70  $\mu\text{m}$  determines the size of the light emitting region. A detailed analysis of the beam diameter requires, however, careful deconvolution of the apparatus profile, the Doppler width, and the broadening caused by the Zeeman-splitting of the spectral lines, since all these factors contribute to the apparent spectral line width. The magnitude of these corrections will now be estimated. First, the imaging system (lenses, prism, windows) has a spatial resolution of 50  $\mu\text{m}$  in the current arrangement, the equivalent of 2 pixels. The Doppler broadening of the lines at ion temperatures typical for EBIT conditions [29,30] is roughly two parts in ten thousand, or 1 Å. With an average dispersion of 5 Å/pixel, this contribution cannot be resolved with the setup described here. The Zeeman splitting of fine structure lines is proportional to the magnetic field and the  $g$ -factor of the corresponding levels. A splitting on the order of 0.2 Å can be expected at the magnetic field value of 3 T at the center of the trap. Such splitting is also unresolvable and is insufficient to explain the difference between the observed spatial and spectral widths.

**Fig. 4.** Spatial width of the spectral lines of different ions. Neutrals reproduce the electron beam width, but highly charged ions spread out of the electron beam. The higher charge states are more tightly bound to the space charge of the electron beam.

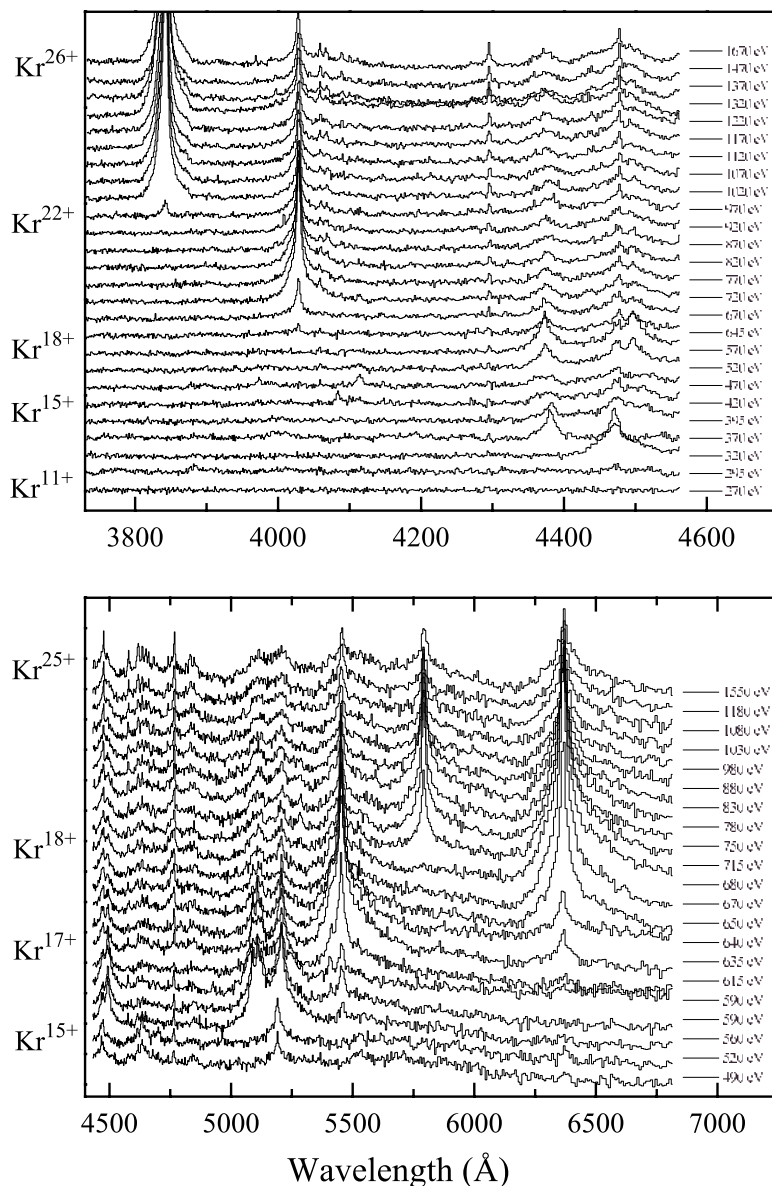


The current density of the electron beam also influences the width of the observed lines. Due to the direct imaging, the spatial distribution of the ions appears in the spectra as source broadening, as shown in Fig. 4. An increase of the electron beam current increases the collisional heating of the ions in the trap [29–30], making the ions spread throughout a wider volume. The data show an ion cloud that can spread as much as  $500\ \mu\text{m}$  to each side of the beam in certain cases. Ions with lower charge states, which are less tightly bound to the electrostatic potential of the trap, showed this behavior more markedly.

The fact that we observed line emission from neutral and singly ionized ions allowed us to establish the wavelength scale of the measurements. The calibration was carried out using lines from neutral and single ionized Kr, Ar, He, and Xe injected into the trap. The usual procedure was to fit a polynomial of third or fourth degree to a set of 20 to 30 calibration lines to account for the nonlinearity of the dispersion of the prism spectrograph. The wavelengths of the calibration lines were taken from ref. 31, and their errors (as low as  $0.01\ \text{\AA}$ ) are negligible (if not misidentified) in comparison with the other experimental uncertainties. The fits delivered typically a standard deviation for the single calibration line of  $3\ \text{\AA}$ . Given that many of these lines appeared as narrow as 2 pixels on our detector, this error is commensurate to their linewidth. The quality of the fit can then be roughly estimated to be on average equal to the standard deviation of the single calibration line divided by the square root of the number of calibration lines, because the number of free parameters on the fit is essentially smaller than the number of calibration lines. This would make the wavelength scale on average good to  $0.6\ \text{\AA}$ , with an uncertainty in the violet at  $3900\ \text{\AA}$  of  $0.3\ \text{\AA}$  and in the red at  $600\ \text{nm}$  of  $1.5\ \text{\AA}$ .

In addition to the calibration uncertainty discussed above, the lines observed for the highly charged ions display a larger line width mainly because of source broadening. This makes the determination of their centroids less precise. In some cases, blends of unknown lines cannot be totally excluded. Let us look at some examples. The  $3962\ \text{\AA}$  line shows a typical width of  $8\ \text{\AA}$ , or about 5 pixels. With this width, the fitting error may be as big as  $2\ \text{\AA}$  ( $1.4\ \text{\AA}/\text{pixel}$  dispersion), which makes the calibration uncertainty of  $0.3\ \text{\AA}$  negligible by comparison. At  $4500\ \text{\AA}$ , the estimated error will be of the order of  $5\ \text{\AA}$ . At  $5420\ \text{\AA}$ ,

Fig. 5. Spectra of Kr ions at different electron beam energies.



the full width half maximum (FWHM) of the line is 20 Å, or roughly 4 pixels; this gives an estimate of the uncertainty of the order of 10 Å. At 6000 Å, the uncertainty can be as high as 15 Å. Again, these large uncertainties are due to the spectral overview character of the present work.

### 3. Results

#### 3.1. Krypton

Krypton spectra covering the region 4500–6900 Å were taken while systematically varying the beam energy from 490 to 1550 eV (Fig. 5). The absolute value of the beam energy is uncertain because of the space charge of the beam electrons. In the present experiments, the magnitude of the space charge was

**Table 1.** Highly charged krypton ions: forbidden lines observed in the visible range and their tentative identifications.

Ion	Seq.	$I_p^{(q-1)+}$ (eV)	$E_{\text{beam}}$ (eV)	$\lambda_{\text{measured}}$ (Å)	Int.	Suggested identification	$\lambda_{\text{pred}}$ (Å)	$gA_{\text{pred}}$ (s <sup>-1</sup> )
Kr <sup>11+</sup>	Mn I	312	320	4478(4)	8	$3d^7\ ^2H_{9/2}-^2G_{9/2}$	4565	340
			360	5527(10)	2	$3d^7\ ^2D_{3/2}-^2P_{3/2}$	5489	210
Kr <sup>12+</sup>	Cr I	353	370	4380(4)	6	$3d^6\ ^3G_3-^3H_4$	4442	80
						$3d^6\ ^3G_4-^3H_5$	5288	70
						$3d^5\ ^2F_{5/2}-^2F_{5/2}$	4239	610
Kr <sup>13+</sup>	V I	397	420	4634(5)	1	$3d^5\ ^2F_{5/2}-^2F_{7/2}$	4563	170
			420	5200(6)	3	$3d^5\ ^2F_{5/2}-^2F_{7/2}$	5300	150
Kr <sup>14+</sup>	Ti I	442	520	4372(4)	6	$3d^4\ ^1G_4-^3G_3$	4451	410
			520	4500(5)	3	$3d^4\ ^3G_5-^3H_5$	4726	220
Kr <sup>15+</sup>	Sc I	490	560	5090(6)	5	$3d^3\ ^2D_{3/2}-^4P_{3/2}$	5068	240
			560	5113(6)	5			
			560	5128(6)	3			
			560	5205(6)	4	$3d^3\ ^2P_{3/2}-^2D_{3/2}$	5235	240
			560	5212(6)	3			
Kr <sup>16+</sup>	Ca I	538	560	<b>5453(10)</b>	15	$3d^2\ ^3P_2-^1D_2$	5397	280
			590	5411(10)	3			
Kr <sup>17+</sup>	K I	588	615	<b>6369(15)</b>	25	$3d^1\ ^2D_{5/2}-^2D_{3/2}$	6387	250
Kr <sup>18+</sup>	Ar I	640	645	<b>4027(2)</b>	30	$3p^5\ 3d^1\ ^3P_2-^3P_1$	4112	970
			715	<b>5793(10)</b>	15	$3p^5\ 3d^1\ ^3F_2-^3F_3$	5660	500
Kr <sup>22+</sup>	Si I	935	970	<b>3843(2)</b>	100	$3p^2\ ^3P_2-^3P_1$	3845	700

**Note:** Ion, ionization stage; Seq., isoelectronic sequence;  $I_p^{(q-1)+}$ , ionization, or energy threshold necessary to produce the ion;  $E_{\text{beam}}$ , energy threshold for the lines observed;  $\lambda_{\text{measured}}$ , observed wavelength; Int, observed relative intensities in arbitrary units;  $\lambda_{\text{pred}}$ , predicted wavelength;  $gA_{\text{pred}}$ , product of the statistical weight  $g = 2J + 1$  and the predicted transition rate  $A_{ik}$ . Strong lines with safe or confirmed identifications are displayed in bold.

not measured. Instead it was estimated from the beam current. This estimate carries an uncertainty of about 40 eV. The relative change in the beam energy is of course known much better. The charge states produced in the trap depend on the electron beam energy and the ionization potential. The trapping times allowed us to reach a narrow steady-state ion charge distribution. Nevertheless, since continuous gas injection was used, a certain amount of ions in lower charges states always appears in the spectra. The highest ionization stages varied according to the beam energy, and we thus observed ions in the charge states from  $q = 14+$  to  $26+$ . In the region 3700–4500 Å, the energy was scanned from 270 to 1670 eV (Fig. 5), and consequently the ionization stage ranged from Kr<sup>11+</sup> to Kr<sup>26+</sup>.

The most prominent features of the spectrum of highly charged Kr are the K-like line at 6369 Å, the Ar-like lines at 4027 and 5793 Å, and the Si-like line at 3843 Å. The lines at 4027 and 3843 Å have been reported earlier by the NIST group [8,9,32] but only the second one had been unambiguously identified.

Table 1 shows a compilation of the measured lines including the threshold beam energy at which the line emerged and their tentative identifications. The tentative identifications are done by comparing the measured wavelengths to those calculated with the Cowan code [33] for the transitions in the ground-state configuration that are expected to occur for the highest charge state produced at a certain beam energy. Assignments of the proper charge state are helped by noting at which beam energy the individual lines appeared. The space charge of the electron beam causes an energy shift that for beam currents of 20–60 mA and beam energies around 1–2 keV (as typical parameters for this work) amounts roughly to 20 to 100 V. So the lines appear always at acceleration voltages higher than the ionization energy needed to produce the ion in question. This effect has been taken into account for the assignments. For weaker

lines, the identifications are only tentative, since the determination of the threshold beam energy is less clear; for strong lines, tests done with argon have shown how the line can be turned on and off with a beam energy variation as little as 3 eV. The ionization stage associated with strong lines is, therefore, well established.

The number of M1 transitions predicted in the visible range is usually a few or none for a particular charge state ground-state configuration. Among the excited states, only the  $3p^53d$  excited configuration in the Ar I isoelectronic sequence shows intense visible lines. Only three levels can decay through an E1 transition to the ground state. M1 and E2 transitions to the ground state are not possible, since the parity of both levels is different. Those with high angular momenta decay instead via an M1 transition within the  $3p^53d^1$  configuration. The  $^3F_2$  and  $^3P_2$  levels from which the transitions start also have M2 transitions to ground state. The M2 transition rates were calculated with the HULLAC code (see Klapisch et al. [34–36]) and are 140 and 480  $s^{-1}$ , respectively. These transition rates have to be compared with 100 and 200  $s^{-1}$ , respectively, for the visible M1 intra-configuration transition from the same upper levels. Therefore, a significant fraction of the level population can decay through the M1 transition without being quenched by the M2 decay, which falls in the soft X-ray region. The M1 and M2 decay channels combined correspond to estimated lifetimes of 3.7 and 1.4 ms. Two levels,  $^3F_4$  and  $^3P_0$ , do not have any radiative E1, M1, E2, or M2 decay channels to the ground state. They are possibly very long lived and are depopulated by collisional mixing with energetically close states only.

The K-like ion  $Kr^{17+}$  line at 6369 Å and the Ca-like ion line at 5453 Å are reasonably well predicted by the code; however, as more and more electrons are added to the *d*-subshell, the identification of the lines becomes more problematic. For instance, in the Sc-like ion  $Kr^{15+}$ , lines expected at wavelengths of 4693, 4722, 4741, 5405, 5420, 5666, and 5702 Å cannot be unequivocally assigned to observed lines, because of the theoretical uncertainties in these wavelengths and the absence of line intensity predictions. These lines will be a challenge for more elaborate atomic structure calculations.

### 3.2. Xenon

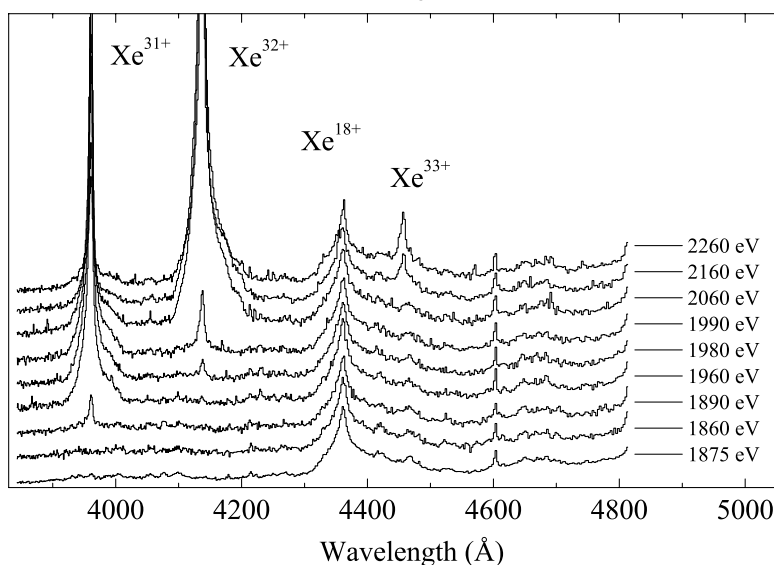
The beam energy was varied between 1650 and 2700 eV to study the ions from  $Xe^{29+}$  to  $Xe^{37+}$  (Mn-like to Cl-like). The observed lines are collected in Table 2. Lines from lower ionization stages and neutral xenon also appear in the spectrum, due to the continuous injection of gas into the trap. A strong transition at 4363 Å (Fig. 6) is tentatively identified as the  $^3P_2-^3P_1$  transition in the first excited configuration  $3s^23p^53d^1$  of the Kr-like ion  $Xe^{18+}$ . At 1770 eV beam energy, a line appears at 5557 Å. The line is also seen in Fig. 3. From this energy threshold it seems likely that this line arises from the Cr-like ion  $Xe^{30+}$ . We do not have a likely identification for this line.

In V-like  $Xe^{31+}$ , a line at 3962 Å, which was first observed by Morgan et al. [8], appears together with a line at 5984 Å. The Cowan code predicts for the  $^4G_{9/2}$  level two possible decay channels with a branching ratio of 1/5: a  $^4G_{9/2}-^4G_{7/2}$  transition at 3944 Å and a  $^4G_{9/2}-^4G_{11/2}$  transition at 6298 Å. We assume, therefore, that the companion line at 5984 Å is the  $^4G_{9/2}-^4G_{11/2}$  transition. The agreement with the prediction seems less good than for the first line, but the long wavelength of the line makes small energy differences in the level calculations a possible explanation. An analogous line found in V-line  $Ba^{33+}$ , again at a shorter wavelength than predicted, might indicate a shift of the  $^4G_{11/2}$  level to lower energies. For the lines registered at the Sc-like, K-like, Ar-like, and Cl-like ionization stages, we do not have tentative identifications, although we have applied the Cowan code to many  $3p^63d^m$  and  $3p^\lambda$  configurations to try to find possible candidate transitions. Possible gas impurities do not seem to be the likely explanation. Other noble gases, such as Kr, Ar, or Ne, do not show these transitions. The trap itself can accumulate heavy ions if the trapping cycle is long, but with continuous gas injection and short dumping cycles we do not observe accumulation of other ions. Transitions between higher Rydberg states, populated by charge exchange or dielectronic recombination, could provide an explanation. However, the lack of such transitions in nearby charge states and the fact that such lines would appear with accompanying lines from the same decay cascade makes this explanation unlikely.

**Table 2.** Highly charged xenon ions: forbidden lines observed in the optical range and tentative identifications.

Ion	Seq.	$I_p^{(q-1)+}$ (eV)	$E_{\text{beam}}$ (eV)	$\lambda_{\text{measured}}$ (Å)	Int.	Suggested identification	$\lambda_{\text{pred}}$ (Å)	$gA_{\text{pred}}$ (s <sup>-1</sup> )
Xe <sup>18+</sup>	Kr I	440	—	4363(4)	5	$4p^5 4d^3 P_2-^3P_1$	4337	750
Xe <sup>30+</sup>	Cr I	1748	1770	5557(10)	4	$3d^6$		
Xe <sup>31+</sup>	V I	1830	1890	<b>3962(2)</b>	50	$3d^5 \ ^4G_{9/2}-^4G_{7/2}$	3944	3110
			1870	<b>5984(10)</b>	10	$3d^5 \ ^4G_{9/2}-^4G_{11/2}$	6298	670
Xe <sup>32+</sup>	Ti I	1920	1960	<b>4139(2)</b>	120	$3d^4 \ ^5D_3-^5D_2$	4052	3160
						$3d^4 \ ^3H_6-^3H_5$	5991	580
Xe <sup>33+</sup>	Sc I	2026	2060	4456(5)	7			
			2080	6327(15)	1			
Xe <sup>35+</sup>	K I	2209	2280	5479(10)	<1			
Xe <sup>36+</sup>	Ar I	2302	2370	4970(6)	<1			
Xe <sup>37+</sup>	Cl I	2565	2650	6066(15)	<1			
			2650	6142(15)	<1			

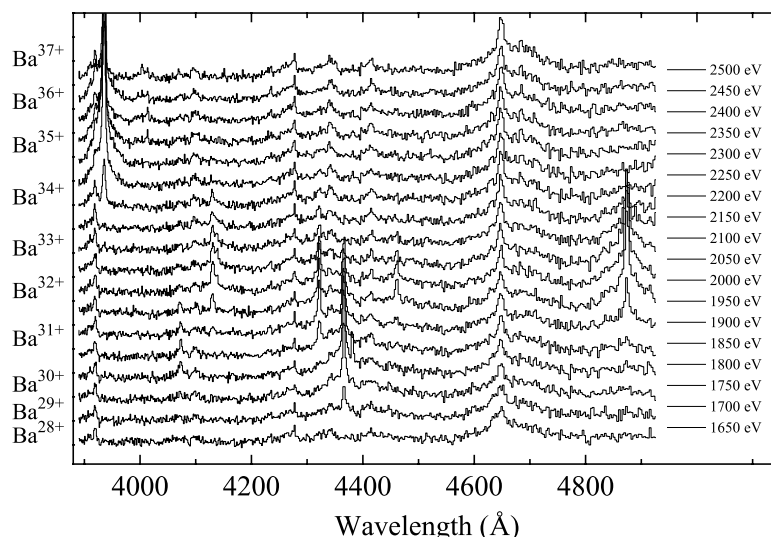
**Note:** Ion, ionization stage; Seq., isoelectronic sequence;  $I_p^{(q-1)+}$ , ionization, or energy threshold necessary to produce the ion;  $E_{\text{beam}}$ , energy threshold for the lines observed;  $\lambda_{\text{measured}}$ , observed wavelength; Int, observed relative intensities in arbitrary units;  $\lambda_{\text{pred}}$ , predicted wavelength;  $gA_{\text{pred}}$ , product of the statistical weight  $g = 2J + 1$  and the predicted transition rate  $A_{ik}$ . Strong lines with safe or confirmed identifications are displayed in bold.

**Fig. 6.** Spectra of Xe taken at different electron beam energies.

### 3.3. Barium

Beam energies between 1650 and 2500 eV allowed us to generate and store ions from Ba<sup>29+</sup> to Ba<sup>36+</sup> (Fig. 7). Barium evaporates slowly from the e-gun cathode and is then trapped if the dumping cycle is long and no other heavy atoms are injected. The lines observed are shown in Table 3. Due to the low influx of neutral Ba into the trap, the charge distribution is more peaked towards the highest charge state produced at a certain beam energy. At the same time, the lower charge states are more depleted or “burned out”.

A number of strong features appear in the spectra. Five observed lines in the Ni I, Co I, and Fe I

**Fig. 7.** Spectra of Ba ions at different electron beam energies.**Table 3.** Highly charged barium ions: forbidden lines observed in the visible range and tentative identifications.

Ion	Seq.	$I_p^{(q-1)+}$ (eV)	$E_{\text{beam}}$ (eV)	$\lambda_{\text{measured}}$ (Å)	Int.	Suggested identification	$\lambda_{\text{pred}}$ (Å)	$gA_{\text{pred}}$ ( $s^{-1}$ )
Ba <sup>28+</sup>	Ni I	984	1700	4366(4)	6	-Pt <sup>37+</sup> ?		
Ba <sup>29+</sup>	Co I	1702	1800	4072(3)	1			—
			1820	4321(3)	3			—
Ba <sup>30+</sup>	Fe I	1788	1870	4128(3)	10	Au <sup>38+</sup> ?		
			1870	4462(4)	2			
			1870	6222(15)	3			
Ba <sup>31+</sup>	Mn I	1875	1900	4873(6)	10	$3d^7 \ ^4F_{5/2} - ^2P_{3/2}$	4749	60
Ba <sup>32+</sup>	Cr I	1964	1970	5681(8)	4	$3d^6 \ ^3D_2 - ^5F_3$	5578	830
			2020	4515(5)	1			
Ba <sup>33+</sup>	V I	2054	2120	4932(7)	3			
			2170	5078(7)	10	$3d^5 \ ^4G_{9/2} - ^4G_{11/2}$	5369	800
Ba <sup>34+</sup>	Ti I	2146	2150	<b>3932(2)</b>	30	$3d^4 \ ^5D_3 - ^5D_2$	3932	3040
			2220	5002(6)	8			
Ba <sup>35+</sup>	Sc I	2259	2350	4019(3)				
Ba <sup>36+</sup>	Ca I	2355	2450	4008(3)				

**Note:** Ion, ionization stage; Seq., isoelectronic sequence;  $I_p^{(q-1)+}$ , ionization, or energy threshold necessary to produce the ion;  $E_{\text{beam}}$ , energy threshold for the lines observed;  $\lambda_{\text{measured}}$ , observed wavelength; Int, observed relative intensities in arbitrary units;  $\lambda_{\text{pred}}$ , predicted wavelength;  $gA_{\text{pred}}$ , product of the statistical weight  $g = 2J + 1$  and the predicted transition rate  $A_{ik}$ . Strong lines with safe or confirmed identifications are displayed in bold.

isoelectronic sequences could not be assigned. Perhaps small Pt and Au impurities present in the trap during the Ba run could explain the observed lines, since there are predicted transitions consistent with the charge states of those elements for these beam energies. A line at 4873 Å could be the  $^4F_{5/2} - ^2P_{3/2}$  transition in the  $3d^7$  configuration in Mn-like Ba<sup>31+</sup>. Cr-like Ba<sup>32+</sup> shows a line at 5681 Å, probably the  $^3D_2 - ^5F_3$  transition in the  $3d^6$  configuration, and an unassigned line at 4515 Å. In the V-like ion, the line at 3436 Å lies outside the spectral range of observation. But another line in the  $3d^5$  configuration

is predicted in the visible range, and we believe it to be the one observed at 5081 Å. The Ti-like Ba<sup>34+</sup> shows a line at 3932 Å, already identified by Morgan et al. [8], as well as an unidentified line at 5002 Å.

#### 4. Summary

A spectrograph for the visible range was set up on the SuperEBIT and EBIT-II electron beam ion traps. Ions of interest corresponding to low-density laboratory and astrophysical sources with open M and L shells have been studied. We measured a total of 11, 15, and 18 lines in the spectrum of highly ionized Xe, Ba, and Kr, respectively. Most of the lines that were assigned were from transitions within the respective ground-state configurations. Visible lines arising from transitions within excited configurations have also been identified in Ar-like Kr<sup>18+</sup>. We have confirmed the three lines reported by Morgan et al. [8] in the visible range and two of the Kr lines reported by Serpa et al. [9]. However, more than half of all lines we observed remain to be assigned. Optical measurements with high-resolution grating spectrographs and implementation of laser spectroscopic techniques into electron beam ion traps will undoubtedly improve the accuracy with which lines are measured in the future, albeit at the expense of wavelength coverage. The present measurements can serve as a broad guide for such experiments.

In most cases, impurities can be excluded as origins of unidentified lines. Transitions between high Rydberg states, fed by charge exchange, could perhaps explain some of the unidentified lines. In the theoretical analysis of the data, further refining of the input parameters could probably improve the agreement with experiment. At this moment, the semiempirical scaling of the  $F^k$  Slater integrals has been employed as the only adjustable theoretical parameter, but the complicated configuration interactions of the open  $d$ -subshell have not been treated properly in this preliminary theoretical analysis, and more elaborate calculations may provide new identifications. The results of this work emphasize the need for dedicated, extensive calculations of the fine structure intervals of the ground state in all diagnostically relevant ions. From the present analysis it is clear that the study of visible lines from highly charged ions is still in its infancy.

#### Acknowledgments

We want to thank Dr. A. Osterheld (LLNL) for help with calculations with the HULLAC code. Discussions with Dr. E. Träbert (Ruhr-Universität Bochum) are gratefully acknowledged. The Steinheil prism spectrograph used in this work was loaned to us by Prof. H. Jäger from the Technische Universität Graz, whom we also wish to thank. This work was performed under the auspices of the U.S. Department of Energy by the University of California Lawrence Livermore National Laboratory under contract W-7405-ENG-48 and was supported in part by the Chemical Sciences, Geosciences, and Biosciences Division of the Office of Basic Energy Sciences, Office of Science, U.S. Department of Energy.

#### References

1. C.A. Young. The sun and the phenomena of its atmosphere. C.C. Chatfield & Co., New Haven, Conn. 1872.
2. P. Swings. *Astrophys. J.* **98**, 119 (1943).
3. W.J. Wagner and L.L. House. *Sol. Phys.* **5**, 55 (1968).
4. S. Suckewer and E. Hinnov. *Phys. Rev. Lett.* **41**, 756 (1978).
5. E. Hinnov. *Nucl. Instrum. Methods*, **202**, 381 (1982).
6. S.I. Lippman, K.B. Fournier, A.L. Osterheld, and W.H. Goldstein. *Phys. Rev. E: Stat. Phys. Plasmas Fluids Relat. Interdiscip. Top.* **51**, 5139 (1995).
7. M.H. Prior. *J. Opt. Soc. Am. B*, **4**, 144 (1987).
8. C.A. Morgan, F.G. Serpa, E. Takacs, E.S. Meyer, J. Sugar, J.R. Roberts, C.M. Brown, and U. Feldman. *Phys. Rev. Lett.* **74**, 1716 (1995).
9. F.G. Serpa, E.W. Bell, E.S. Meyer, J.D. Gillaspay, and J.R. Roberts. *Phys. Rev. A: At. Mol. Opt. Phys.* **55**, 1832 (1997).

10. D.J. Bieber, H.S. Margolis, P.K. Oxley, and J.D. Silver. *Phys. Scr. T*, **73**, 64 (1997).
11. E. Träbert, P. Beiersdorfer, S.B. Utter, and J.R. Crespo López-Urrutia. *Phys. Scr.* **58**, 599 (1998).
12. S.B. Utter, P. Beiersdorfer, and G.V. Brown. *Phys. Rev. A: At. Mol. Opt. Phys.* **61**, 030503 (2000).
13. J.V. Porto, I. Kink, and J.D. Gillaspay. *Phys. Rev. A: At. Mol. Opt. Phys.* **61**, 054501 (2000).
14. D.E. Post. *J. Nucl. Mater.* **222**, 143 (1995).
15. J. Mandrekas, W.M. Stacey, and F.A. Kelly. *Contrib. Plasma Phys.* **2–3**, 245 (1996).
16. M. Bitter, H. Hsuan, K. Hill, R. Hulse, M. Zarnstropp, and P. Beiersdorfer. *In Atomic and plasma-material interaction processes in controlled thermonuclear fusion. Edited by R.K. Janev and H.W. Drawin. Elsevier, Amsterdam. 1993. pp. 119–133.*
17. P. Beiersdorfer, R. Cauble, S. Chantrenne, M.H. Chen, N. DelGrande, D.A. Knapp, R.E. Marrs, A. Osterheld, K. Reed, M.B. Schneider, J. Scofield, B. Wargelin, K. Wong, D.A. Vogel, and R. Zasadzinski. *In UV and X-ray spectroscopy of astrophysical and laboratory plasmas. Edited by E. Silver and S. Kahn. Cambridge University Press, Cambridge. 1993. p. 59–68.*
18. B. Wargelin, P. Beiersdorfer, and S. Kahn. *Phys. Rev. Lett.* **71**, 2196 (1993).
19. P. Beiersdorfer, T.W. Phillips, K.L. Wong, R.E. Marrs, and D.A. Vogel. *Phys. Rev. A*, **46** 3812 (1992).
20. J.R. Crespo López-Urrutia, P. Beiersdorfer, D.W. Savin, and K. Widmann. *Phys. Rev. Lett.* **77**, 826 (1996).
21. J.R. Crespo López-Urrutia, P. Beiersdorfer, K. Widmann, B.B. Birkett, A.-M. Mårtensson-Pendrill, and M.G.H. Gustavsson. *Phys. Rev. A: At. Mol. Opt. Phys.* **57**, 879 (1998).
22. E. Träbert, S.B. Utter, and P. Beiersdorfer. *Phys. Lett.* **272A**, 86 (2000).
23. H. Chen, P. Beiersdorfer, C.L. Harris, and S.B. Utter. *Phys. Scr.* Submitted.
24. E. Träbert, P. Beiersdorfer, and S.B. Utter. *Phys. Scr. T*, **80**, 450 (1999).
25. E. Träbert, P. Beiersdorfer, G.V. Brown, H. Chen, D.B. Thorn, and E. Biéumont. *Phys. Rev. A: At. Mol. Opt. Phys.* **64**, 042511 (2001).
26. J.R. Crespo López-Urrutia, P. Beiersdorfer, and K. Widmann. 19th International Conference on the Physics of Electronic and Atomic Collisions ICPEAC, 26 July–1 August 1995. Whistler, B.C. Book of Abstracts, Vol. 2, p. 589.
27. M.A. Levine, R.E. Marrs, J.N. Bardsley, P. Beiersdorfer, C.L. Bennet, M.H. Chen, T. Cowan, D. Dietrich, J.R. Henderson, D.A. Knapp, A. Osterheld, B.M. Penetrante, M.B. Schneider, and J.H. Scofield. *Nucl. Instrum. Methods, Phys. Res. Sect. B*, **43**, 431 (1989).
28. D.A. Knapp, R.E. Marrs, S.R. Elliot, E.W. Magee, and R. Zasadzinsky. *Nucl. Instrum. Methods, Phys. Res. Sect. A*, **334**, 305 (1993).
29. P. Beiersdorfer, A.L. Osterheld, V. Decaux, and K. Widmann. *Phys. Rev. Lett.* **77**, 5353 (1996).
30. P. Beiersdorfer, V. Decaux, S.R. Elliott, K. Widmann, and K. Wong. *Rev. Sci. Instrum.* **66**, 303 (1995).
31. J. Reader and C.H. Corliss. Wavelengths and transition probabilities for atoms and atomic ions. U.S. Department of Commerce, National Bureau of Standards, Washington, D.C. Publication NSRDS-NBS 68, 1980.
32. F.G. Serpa, E.S. Meyer, C.A. Morgan, J.D. Gillaspay, J. Sugar, J.R. Roberts, C.M. Brown, and U. Feldman. *Phys. Rev. A: At. Mol. Opt. Phys.* **53**, 2220 (1996).
33. R.D. Cowan. *The theory of atomic structure and spectra. University of California Press, Berkeley, Calif. 1981. p. 456.*
34. M. Klapisch. *Comput. Phys. Commun.* **2**, 239 (1971).
35. M. Klapisch, J.L. Schwab, B.S. Fraenkel, and J. Oreg. *J. Opt. Soc. Am.* **67**, 148 (1977).
36. A. Bar-Shalom, M. Klapisch, and J. Oreg. *Phys. Rev. A: Gen. Phys.* **38**, 1773 (1988).